Chinese Chemical Letters 36 (2025) 109587

Contents lists available at ScienceDirect

Chinese Chemical Letters

journal homepage: www.elsevier.com/locate/cclet

Improving performance of perovskite solar cells enabled by defects passivation and carrier transport dynamics regulation *via* organic additive

Rongjun Zhao[a,b], Tai Wu[b], Yong Hua[b,*], Yude Wang[c,*]

[a] *Department of Physics, Center for Optoelectronics Engineering Research, Yunnan University, Kunming 650091, China*
[b] *Yunnan Key Laboratory for Micro/Nano Materials & Technology, International Joint Research Center for Optoelectronic and Energy Materials, School of Materials and Energy, Yunnan University, Kunming 650091, China*
[c] *Yunnan Key Laboratory of Carbon Neutrality and Green Low-carbon Technologies, Yunnan University, Kunming 6500504, China*

ARTICLE INFO

Article history:
Received 1 January 2024
Revised 19 January 2024
Accepted 29 January 2024
Available online 6 February 2024

Keywords:
Perovskite solar cells
Additives
Defects passivation
Carrier dynamics
Stability

ABSTRACT

Defects at the grain boundaries (GBs) of perovskite film highly restrict both the efficiency and stability of perovskite solar cells (PSCs). Herein, organic small molecules of butanedioic acid (BA) and acetylenedicarboxylic acid (AA), containing two carbonyl (C=O) groups and different core-units, were incorporated into perovskite as additives for PSCs application. Thanks to the strong coordination interaction between C=O group and under-coordinated Pb^{2+}, the additives can effectively passivate film defects and regulate the perovskite crystallization, yielding high-quality perovskite films with lower defect densities. More importantly, the additives can efficiently regulate the charge transport behaviors in PSCs. Benefiting from the defects passivation and the regulation of charge carrier dynamics, the BA and AA-treaded PSCs show the power conversion efficiencies of 21.52% and 20.50%, which are higher than that of the control device (19.41%). Besides, the optimal devices exhibit a remarkable enhanced long-term stability and moisture tolerance compared to the pristine devices. Furthermore, the transient absorption spectrum reveals the mechanism of enhanced photovoltaic performances, attributing to the improvement of charge transport capability at the perovskite/Spiro-OMeTAD interfaces. This work affords a promising strategy to improve the efficiency and stability of PSCs through regulating the charge-carrier dynamic process in perovskite film.

In the past decades, organic-inorganic hybrid perovskite solar cells (PSCs) have gained extensive attention in the next generation of photovoltaic devices owing to their superior advantages, such as high light-absorption coefficient, high carriers mobility, low recombination rate, adjustable bandgap, low exciton binding energy and low-cost solution-process fabrication, *etc*. [1–7]. Up to now, many efforts have been devoted to further improve the photovoltaic properties and recently a certified record power conversion efficiency (PCE) exceed 26% was achieved in single-junction PSCs [8], which is comparable with the crystalline-silicon solar cells. However, numerous inevitable defects formed at the GBs during the solution-processed polycrystalline perovskite films and post-heat treatment [9–11]. Those defects (such as under-coordinated Pb^{2+} and GBs) not only induce serious charge-carrier non-radiative recombination but also provide channels for moisture/oxygen infiltration, which extremely reducing the efficiency and stability of PSCs and hinders their commercial application [12–16]. Therefore, the effective defect passivation and high-quality perovskite films are critical to achieve the highly-efficient and stable PSCs. Recently, various strategies have been employed to regulate the quality of perovskite films, passivate defects and improve the charge transportation ability to boost the efficiency and stability of PSCs, such as interfacial modification [17], composition modulation [18], green-solvent engineering [19], 2D/3D heterojunction [20] and additive engineering [21,22]. Among them, additive engineering has been confirmed as a feasible and effective strategy for defect passivation and crystallinity regulation in perovskite [23]. Up to date, various additive materials with different structural features and functional groups have designed and employed to improve the photovoltaic performances of PSCs.

To the best of our knowledge, under-coordinated Pb^{2+} and GBs related traps are the dominate recombination centers in perovskite film, which impedes the enhancement of efficiency and stability

* Corresponding authors.
E-mail addresses: huayong@ynu.edu.cn (Y. Hua), ydwang@ynu.edu.cn (Y. Wang).

https://doi.org/10.1016/j.cclet.2024.109587
1001-8417/

[16]. Considering the Lewis acid nature of PbI_2, Lewis bases additives with various functional groups (such as N-, S-, P- and O) are widely employed to bond with under-coordinated Pb^{2+} and form the Lewis acid-base adducts *via* strong coordination reaction, leading to the reduction of defects-induced charge nonradiative recombination and the formation of high-quality perovskite film [24–27]. For example, Tan *et al.* introduced Lewis base additive of ethyl 2-(2-aminothiazole-4-yl)-2-hydroxyiminoacetate (EHA) into PbI_2 precursor, which can passivate both Pb-I anti-site and iodine vacancy defects and promote the charge transfer, resulting in the champion efficiency of 24.1% and excellent humidity and thermal stability of devices [28]. Liu *et al.* incorporated the multifunctional additive of BBF complex that contains both C_7H_9N and BF_3 groups into perovskite precursor, the groups separately bond with under-coordinated Pb^{2+}/I^- and FA^+, which achieves the passivation of both cation and anion defects derived from perovskite. The synergistic effect of Lewis base and Lewis acid groups improved the stability and the efficiency of PSCs exceeding 23% [29]. Owing to the excellent passivation effect of carbonyl group and the hydrophobic characteristic of long alkyl chain, Chen's group reported that the introduction of 11Maleimidoundecanoic acid (11MA) additive molecule effectively reduced the trap-states density and inhibited ion migration in perovskite film, thus effectively enhancing the efficiency and stability of tri-cation based hybrid PSCs [30]. Besides, the antisolvent additive engineering (AAE) strategy has been utilized to heal the trap states derived from perovskite [31,32]. Among various electron-donors, the carbonyl (C=O) functional group has been proven that enormous potential to passivate defects owing to the strong electronegativity of oxygen atom. Although great improvements in PSCs have been achieved by introducing additive materials, the influences of different additive structures on the charge-carrier kinetics in shorter timescale still lack systematic explorations.

Recognizing the strong passivation effect of C=O group, two carbonyl-containing flexible small organic molecular additives with different core units, named butanedioic acid (BA) and acetylenedicarboxylic acid (AA), were designed to optimize the photovoltaic properties of PSCs. Furthermore, we have investigated the possible structure-activity relationship between molecular structures and optoelectronic properties. With the introduction of additives, the coordination interaction between Pb^{2+} and C=O groups effectively modulates the crystal growth kinetics and promotes the formation of high-quality perovskite films with smooth and pinhole-free surface, which are beneficial to reduce the defects density. As a consequence, the PCE significantly improved from 19.41% (control) to 21.52% and 20.50% after treatment with BA and AA, respectively. Particularly, the BA-treated device reveals excellent stability and the efficiency still remains 93.7% of initial PCE after aging over 1100 h. In addition, the charge carrier transfer photophysical process were deeply investigated by transient absorption (TA) spectroscopy.

Fig. 1a depicts the molecular structures of organic molecular additives with different core-unit of C–C and C≡C bond for BA and AA that contain two terminal carbonyl groups. As a typical high electrons density group, C=O groups can coordinate with under-coordinated Pb^{2+} by donating isolated electrons pairs, achieving effective defects passivation and crystallization regulation [33]. The possible formation mechanism of perovskite films with molecular additives are shown in Fig. 1b. Generally, the perovskite shows rapid nucleation and crystallization under the post-annealing treatment, thus, it is easy to form the poor-quality perovskite films that containing pinholes, more grain boundaries and excessive under-coordinated Pb^{2+} defects, which would cause charge recombination and energy loss in PSCs. On the contrary, the strong coordination interaction between C=O group and Pb^{2+} may retard the perovskite crystallization, thereby promoting the preferential orientation and uniform growth of perovskite films.

To identify the effects of additives on the crystallinity and growth of perovskite films, XRD characterizations were conducted and shown in Fig. 1c. It can be found that all samples exhibit typical diffraction peaks at 14.12°, 28.42° and 31.78°, which are separately assigned to the (110), (220) and (310) crystal planes of perovskite films [13,34]. Noticeably, the diffraction peaks at 12.83 degree arising from the residual PbI_2 has been effectively suppressed after incorporating additives compared with the pristine film, demonstrating that organic small molecules treatment shows a positive effect on inhibiting traps formation [23]. More importantly, no distinct peaks shift and other character peaks are detected after incorporating additives. As shown in Fig. S1 (Supporting information), the full width half-maximum (FWHM) of (110) peak at 14.12° decreased from 0.141 (control) to 0.126 (BA-treated perovskite), demonstrating that the introduction of BA can effectively regulate the crystallization process of perovskite, promoting the formation of high-quality perovskite film with large grain sizes, thus reducing the film defects. Furthermore, the ultraviolet-visible (UV–vis) absorption spectrum characterization was performed (Fig. 1d). Clearly, all films exhibit a similar UV–vis absorption spectrum with an optical absorption edge around 785 nm, particularly, the BA and AA-treated perovskite films have much stronger light absorption intensity compared with the bare film, which is ascribed to the better quality of perovskite films. Meanwhile, the optical bandgap (E_g) of bare and additive-treated films were estimated by the corresponding Tauc plot and displayed in Fig. S2 (Supporting information). The calculated bandgaps were about 1.56, 1.56 to 1.57 eV for bare, BA and AA-treated perovskite films, respectively. The results indicate that the molecular additives passivation treatment show a negligible impact on the intrinsic bandgaps of perovskite.

To verify the interaction mechanism and the surface chemical states of perovskite films upon BA and AA additives, X-ray photoelectron spectroscopy (XPS) analysis was conducted. Fig. S3a (Supporting information) displays the high-resolution XPS spectra of Pb 4f orbit. In the control sample, two distinct symmetric characteristic peaks located at 143.31 eV and 138.46 eV are separately assigned to the Pb $4f_{5/2}$ and Pb $4f_{7/2}$, the difference value of spin-orbit binding energy consistent with the previous results and suggests that the lead element existed in the form of Pb^{2+} and the under-coordinated Pb^{2+} are dominate trap-states in perovskite film [35,36]. Obviously, the characteristic peaks of Pb 4f shift toward the lower binding energy after additives treatment, the corresponding binding energy shift are about 0.22 eV and 0.08 eV for BA and AA-treated perovskite films, confirming that the C=O groups bond with under-coordinated Pb^{2+} *via* donating lone pair electrons and changes the electron cloud density around Pb ions. Notably, the large shift of Pb 4f peak demonstrates that the BA molecule shows a stronger coordination effect on under-coordinated Pb^{2+} defects than that of AA additive, which would be more efficient in improving the photovoltaic performances. Meanwhile, the I 3d core-level measurement also exhibits the similar change tendency for additive-treated perovskite films (Fig. S3b in Supporting information) [36]. The XPS measurement confirms that the Lewis base C=O groups effectively passivated under-coordinated Pb^{2+} defects. Additionally, the FTIR characterizations were performed to deeply verify the specific interactions between the additives and PbI_2 (Figs. S4 and S5 in Supporting information). As shown in the magnified FTIR spectra (Fig. S5), the characteristic peaks located at 1708.4 and 1703.1 cm^{-1} were assigned to the stretching vibration of C=O in BA and AA molecules, respectively. Surprisingly, the C=O vibration peaks from additive-PbI_2 complex undergo a distinct shift to 1696.1 and 1692.5 cm^{-1}, signifying the interaction between additive molecules and Pb^{2+} [13,28].

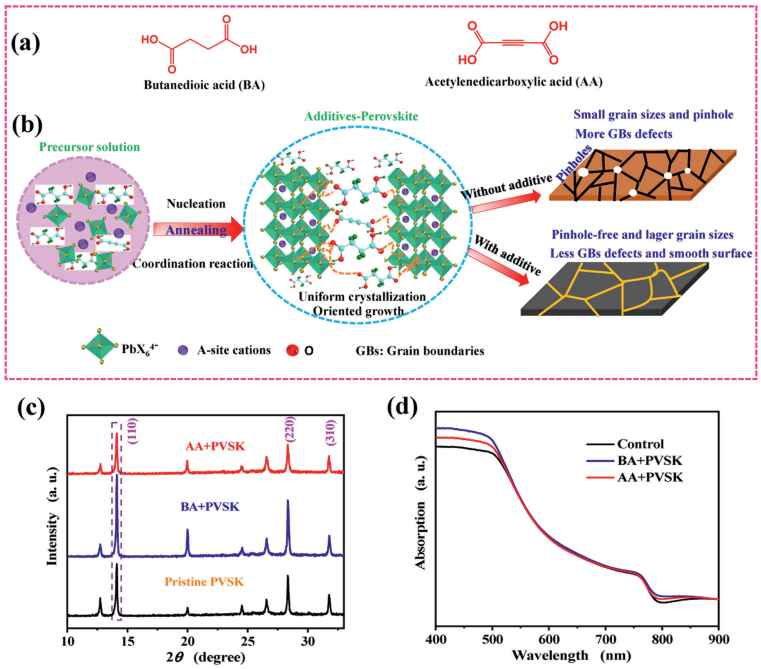

Fig. 1. (a) The chemical structure of BA and AA, respectively. (b) Schematic diagram of the possible perovskite crystal growth and film formation with various additive molecules. (c) The XRD patterns and (d) UV-vis absorption spectra of additives-treated perovskite films, respectively.

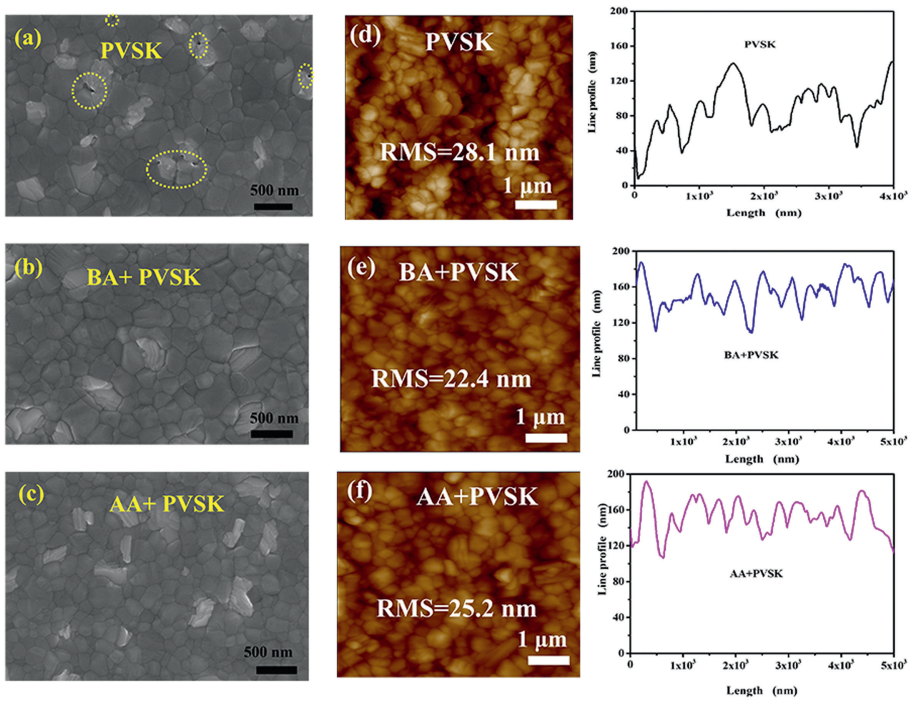

Fig. 2. (a–c) FESEM images and (d-f) AFM images of pristine, BA and AA additives-treated perovskite films deposited on glass substrates, respectively.

To further investigate the impact of additives on the perovskite film quality, the FESEM measurements were conducted to evaluate the surface morphology of perovskite films. As shown in the top-view FESEM images (Figs. 2a–c), some pinholes and cracks are observed on the pristine perovskite surface, which is not good for the efficiency and stability of PSCs. After introducing BA and AA additives, the perovskite films show homogeneous, smooth and pinhole-free morphology. Especially, the BA treated films show enhanced grain sizes. These results confirm that the strong coordination reaction between Pb^{2+} ions and C=O group can bridge the adjacent perovskite grains and effectively retard the crystallization rate during the growth process, thereby reducing the traps of perovskite films. Then, atomic force microscopy (AFM) were implemented to study the surfacial microstructures of perovskite films without and with additives (Figs. 2d–f). As expected, more smooth and dense surface are achieved in BA and AA doped perovskite films, the corresponding root mean square (RMS) roughness were significantly decreased from 28.1 nm (pristine film) to 22.4 nm (BA-treated film) and 25.2 nm (AA-treated film), respectively. Therefore, high-quality perovskite film not only can reduce

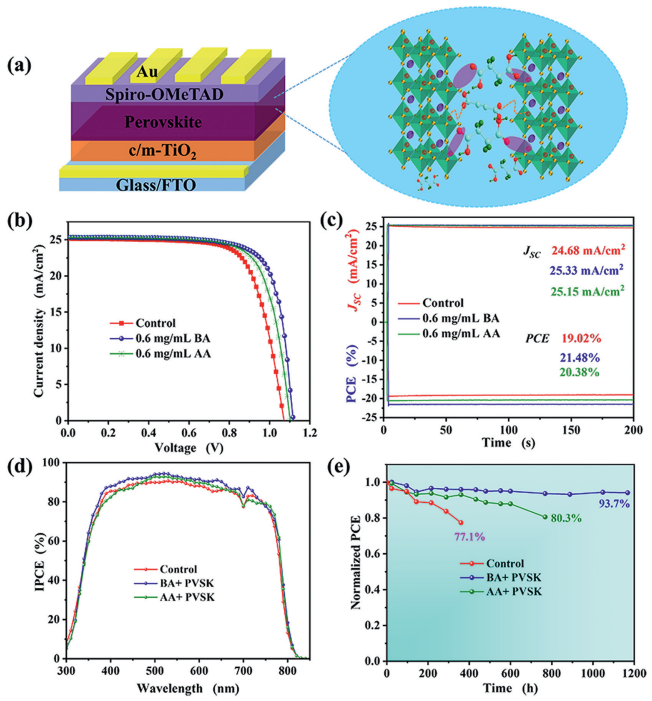

Fig. 3. (a) The fabricated PSC device configuration. (b) The typical *J–V* curves of solar cells based on different additives with optimal concentration. (c) The steady-state output of photocurrent and PCE at maximum power point. (d) IPCE spectra of PSCs devices. (e) The long-term stability of unencapsulated devices based on optimal concentration stored in room temperature and ~40% relative humidity.

Table 1
The photovoltaic performances of perovskite solar cells based on different additives with the optimal concentration.

Devices	J_{SC} (mA/cm^2)	V_{OC} (V)	FF (%)	PCE (%)
Control	25.17	1.07	72.06	19.41
BA	25.36	1.12	75.75	21.52
AA	25.29	1.10	73.68	20.50

the defects density but also improve the interfacial charge transfer and extraction, which is beneficial to enhancing PSCs performance.

The solar cells with n-i-p planar configuration of FTO glass/c-TiO_2/m-TiO_2/perovskite with or without additives/Spiro-OMeTAD/Au (Fig. 3a) were fabricated to evaluate the impacts of additives on the photovoltaic performance. To optimize the gradient concentrations conditions, the comparative experiments of different concentration additives treated PSCs were performed. The current density-voltage (*J-V*) curves were measured under AM 1.5G illumination, as shown in Fig. S6 (Supporting information), the corresponding photovoltaic parameters are listed in Tables S1 and S2 (Supporting information). Obviously, PCE values were increased with the additives concentration increasing, the best efficiencies were obtained at the optimal concentration of 0.6 mg/mL and 0.6 mg/mL toward BA and AA additives, respectively. Conversely, the performances of devices gradually decreased with further adding the additives. According to the *J-V* curves of best-performing devices showed in Fig. 3b, the PCE values were enhanced to 21.52% and 20.50% for BA and AA-treated devices, respectively, which are higher than that of control device (19.41%), Table 1 summaries the detailed photovoltaic parameters. Among them, the BA-treated device obtains the highest PCE values with a greatly enhanced photocurrent density (J_{SC}) of 25.36 mA/cm^2, high V_{OC} of 1.12 V and *FF* of 75.75%, which are obviously higher than that of the control device with J_{SC} of 25.17 mA/cm^2, V_{OC} of 1.07 V and *FF* of 72.06%.

Additionally, the statistical PCE of 20 devices for different PSCs are shown in Fig. S7 (Supporting information). The results reveal that the BA-treated devices exhibit a higher PCE with better reproducibility than that of the control devices. Subsequently, the steady-state power output of solar cells was measured through tracking the maximum power point (MPP) under continuous 1 sun illumination for 200 s. As displayed in Fig. 3c, the stabilized J_{SC} outputs of 24.68, 25.33 and 25.15 mA/cm^2 were obtained for control, BA and AA-treated devices, the corresponding stabilized PCE are 19.02%, 21.48% and 20.38% under the biased at 0.822, 0.934 and 0.906 V, respectively. The results demonstrate that the devices exhibit good light-soaking stability. To further explore the photocurrent response characteristics of solar cells, the incident photo-to-electron conversion efficiency (IPCE) spectra of PSCs were tested in the wavelength range of 300–850 nm (Fig. 3d). Obviously, all devices exhibit a good photoresponse characteristics in the visible spectrum. Among them, the BA-treated champion device shows a significant improvement of IPCE intensity and strong light-harvesting capability in the same spectrum range, demonstrating better quality of perovskite films.

Then, we further evaluate the long-term stability of unencapsulated devices stored at a relative humidity (RH) of ~40% and room temperature condition. As depicted in Fig. 3e, the PCE of control device sharply dropped to the 77.1% of initial PCE value after storing ~360 h. However, the optimized devices with BA and AA treatment exhibit obvious enhancement of stability, the BA and AA-treated devices separately remain 93.7% and 80.3% of their initial PCE values after aging for 1160 h and 760 h, respectively. The excellent stability can be attributed to the better quality of perovskite films. Furthermore, the water contact angle (WCA) measurements were carried out to assess the hydrophobicity nature of perovskite films without and with additives, as shown in Fig. S8 (Supporting information). Clearly, the WCA is increased from 68° (control) to 76° (BA-treated perovskite) and 71° (AA-treated perovskite), respectively, revealing the improved hydrophobicity of perovskite films treated by molecular additives, particularly BA treatment, which is beneficial for the enhancement of moisture tolerance of perovskite.

To get insight into the charge-carrier kinetics of perovskite induced by additives, the steady-state photoluminescence (PL) and time-resolved PL (TRPL) were performed with excitation light of 475 nm. As shown in Fig. S9 (Supporting information), the PL intensity of additives-treated perovskite films significantly enhanced in the order of BA>AA>control, demonstrating that the flexible small organic molecules can effectively suppress charge nonradiative recombination *via* coordination reaction between C=O groups and under-coordinated Pb^{2+} [37]. Furthermore, the TRPL decay curves of perovskite films were fitted by bi-exponential function (Fig. S10 in Supporting information) and the average lifetime (τ_{ave}) were calculated by the following equations, and the fitted parameters were tabulated in Table S3 (Supporting information) [36]:

$$I(t) = A_1\exp(-t/\tau_1) + A_2\exp(-t/\tau_2) \quad (1)$$

$$\tau_{ave} = \left(A_1\tau_1^2 + A_2\tau_2^2\right)/(A_1\tau_1 + A_2\tau_2) \quad (2)$$

Obviously, τ_{ave} was greatly increased from 41.10 ns (control) to 975.84 ns and 117.75 ns for the BA and AA treated perovskite films, respectively. Especially, the BA-treated perovskite film exhibits the prolonger charge lifetime than that of other films [38]. Additionally, the differences in charge recombination dynamics within the devices were reflected by the transient photovoltage (TPV) decay behaviors. As shown in Fig. S11 (Supporting information), the TPV decay lifetimes are elongated from 389.58 ms (control) to 779.15 ms (BA-treated device) and 516.05 ms (AA-treated device), respectively, which implying the conspicuous reduction of

the charge recombination in device. These results confirm that the charge recombination can be more efficiently suppressed in BA treated PSCs, which is responsible for the improvement of V_{OC}, FF and PCE [39,40].

Moreover, the trap-state density (N_{trap}) of perovskite films with and without additives passivation were quantitatively evaluated by the space-charge-limited current (SCLC) method with the electron-only structure with FTO/TiO_2/perovskite/PCBM/Au. As shown in Fig. S12 (Supporting information), the bias voltage at the inflection point between the Ohmic regime and the trap-filled limited (TFL) regime was recognized as the trap-filled limited voltage (V_{TFL}), the N_{trap} can be deduced from V_{TFL} by the equation $N_{trap} = (2\varepsilon\varepsilon_0 V_{TFL})/(eL^2)$ [28]. Accordingly, the calculated N_{trap} values are 1.48×10^{16} cm^{-3} and 4.82×10^{16} cm^{-3} for BA and AA passivated devices, which are much lower than that of control device (5.76×10^{16} cm^{-3}). The reduction of trap-state density implies that the introduced flexible molecular additives could effectively passivate perovskite defects, reducing the channels of moisture or oxygen permeation, and thus improving the efficiency and stability of PSCs. To deeply understand the charge recombination and the improved photovoltaic properties, the dependences of V_{OC} and J_{SC} on different light intensity were investigated. Obviously, the slope values of V_{OC} *versus* light intensity for BA and AA-treated devices were separately extracted to be 1.61 KT/q and 1.87 KT/q, which are much lower than that of the control device (2.94 KT/q) (Fig. S13 in Supporting information). The results prove that the trap-induced Shockley-Read-Hall (SRH) recombination is effectively suppressed in additives treated devices, resulting in the enhancement of V_{OC} and *FF* [41]. Fig. S14 (Supporting information) presents the dependence of J_{SC} on various light intensity (I) and follows the power law of $J_{SC} \propto I^{\alpha}$, where α equal to 1 indicates the inhibited radiative recombination in devices [42]. Clearly, the α values of control, BA and AA-treated devices are 0.987, 0.998 and 0.995, respectively, illustrating that the bimolecular recombination at the interface is well restricted in BA-treated PSCs, thus, effectively improving photovoltaic performance.

To deeply understand the influences of additives on the photogenerated carrier transfer and recombination behaviors in device, the nanosecond transient absorption spectroscopy (ns-TAS) were characterized. Fig. S15 (Supporting information) depicts the ns-TAS of pristine, BA and AA-treated PVSK/Spiro-OMeTAD films at specific delay times from 50 ns to 1 μs. Obviously, a positive photo-induced absorption (PIA) peak at around 500–600 nm and a strong negative photobleaching (PB) peak at around 780 nm are presented for all samples under pump-laser excitation [43,44]. Furthermore, the peaks are clearly showed in the corresponding 2D *pseudo*-color plot of ns-TAS (Fig. S16 in Supporting information). According to the previous reports, the PIA characteristic peak can be associated with the transient species absorption. The strong negative PB signal at around 780 nm can be related to the bandgap renormalization process and exciton transition of perovskite/Spiro-OMeTAD films [43]. From the respective ns-TAS spectra, we find that the intensities of negative PB signals distinctly decreased with further increasing delay time from 50 ns to 1 μs for all samples. As shown in Fig. S17 (Supporting information), the decay curves were fitted by a typical bi-exponential functions, τ_{ave} of BA and AA-treated PVSK/Spiro-OMeTAD films are separately calculated to be 4867.85 ns and 4400.26 ns, which are much higher than that of pristine PVSK/Spiro-OMeTAD film (2785.97 ns) (fitted parameters are listed in Table S4 in Supporting information). More importantly, the interfacial charge recombination velocity (defined as K) was estimated by the equation of $K = 1/\tau$, which decreased from 3.59×10^5 s^{-1} (PVSK/Spiro-OMeTAD) to 2.0×10^5 s^{-1} (BA+PVSK/Spiro-OMeTAD) and 2.27×10^5 s^{-1} (AA+PVSK/Spiro-OMeTAD), confirming that the interfacial charge recombination is significantly suppressed in BA-treated device [37,43,44].

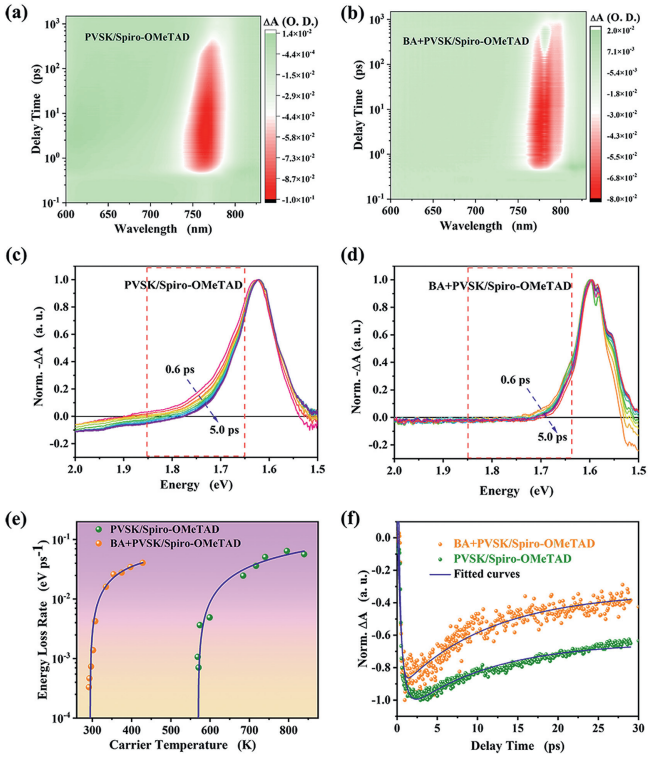

Fig. 4. 2D *pseudo*-color plots of fs-TA for (a) PVSK/Spiro-OMeTAD and (b) BA+PVSK/Spiro-OMeTAD. The normalized fs-TA spectrum of (c) PVSK/Spiro-OMeTAD and (d) BA+PVSK/Spiro-OMeTAD. (e) Energy loss rate of different samples. (f) The normalized fs-TA kinetic of PVSK/Spiro-OMeTAD without and with BA additives.

To systemically investigate the charge-carrier dynamic process induced by additives in shorter timescale of picosecond or femtosecond, the femtosecond transient absorption (fs-TA) spectrum measurements for PVSK/Spiro-OMeTAD and BA+PVSK/Spiro-OMeTAD films were conducted. In this work, a pump energy of 2.61 eV (photoexcitation wavelength about 475 nm) was used to excite samples. Figs. 4a and b illustrate the typical 2D *pseudo*-color fs-TA plots of PVSK/Spiro-OMeTAD and BA+PVSK/Spiro-OMeTAD films. Obviously, a strong negative ($\triangle A < 0$) photobleaching (PB) signal located at approximately 775 nm is observed for both samples, which originates from the ground-state bleaching (GSB) band due to the band-filling effect of free carriers. Figs. 4c and d show the corresponding normalized fs-TA spectrum at early delay time from 0.6 ps to 5.0 ps after photoexcitation. Owing to the rapid transition from initial *quasi*-equilibrium carriers distribution to a Fermi-Dirac distribution of hot carriers *via* elastic scatterings, the broadening behavior of PB features in high energy tail region can be seen for all samples [45–48]. Compared with PVSK/Spiro-OMeTAD film, the broadening of the high energy tail gradually narrows with delay time in BA+PVSK/Spiro-OMeTAD films, signifying the hot carriers rapidly cool down to the perovskite crystal lattice and efficiently transport from BA-treated perovskite to Spiro-OMeTAD, which can be characterized by the hot carrier temperature (T_C) [47,48].

Herein, we evaluated the evolution of T_C as a function of delay time for both sample that extracted from the representative fs-TA spectrum. According to the previous literatures, the T_C values can be obtained by fitting the high energy tails of PB signal above band edge followed the Maxwell-Boltzmann (MB) distribution function, as described as following [49,50]:

$$\Delta A(h\omega) = -A_0 \exp^{(-h\omega/(K_B T_C))} \quad (3)$$

where $\triangle A$ represents the amplitude of PB signal at a probe wavelength, K_B and T_C are Boltzmann constant and hot carrier temperature, respectively. As depicted in Fig. S18 (Supporting information), the initial carrier temperatures were calculated to be 839 K and 428 K for PVSK/Spiro-OMeTAD and BA+PVSK/Spiro-OMeTAD films, respectively, indicating that the BA additive shows an influence on the hot carrier cooling dynamics. Clearly, the PVSK/Spiro-OMeTAD film exhibits slower hot carrier cooling process with delay time as longer as ~1.02 ps, conversely, the hot carrier rapidly cooling down approximately to room temperature within ~363 fs for BA+PVSK/Spiro-OMeTAD film. Such rapid T_C evolution process demonstrates that hot holes and related excess energy can be more efficiently transferred from BA-treated PVSK film to Spiro-OMeTAD hole transport layer (HTL) before them completely thermalize to the equilibrium with perovskite lattice, thereby reducing the interfacial charge recombination, subsequently resulting in the achievement of highly efficient and stable PSCs devices [46–48].

In order to reveal the influence of BA on the energy loss of devices, the energy loss rate per carrier (J_r) is employed to assess it, which can be obtained from T_C evolution curves by the equation of $J_r = -1.5K_B(dT_C/dt)$ [47,51]. Fig. 4e displays the carrier temperature dependent J_r values for PVSK/Spiro-OMeTAD and BA+PVSK/Spiro-OMeTAD film. Noticeably, the energy loss rate of BA+PVSK/Spiro-OMeTAD film is much larger than that of PVSK/Spiro-OMeTAD film, signifying that more efficient hot holes transportation and extraction at the BA+PVSK/Spiro-OMeTAD interface. Moreover, the normalized PB recovery kinetics of fs-TA spectrum was developed to analyze the interfacial hot carrier cooling and extraction (Fig. 4f). The hot carrier kinetic profiles curves were fitted by a three-exponential function and the results are summarized in Table S5. We found that the average HCs cooling time of PVSK/Spiro-OMeTAD film is 9.25 ps, which is reduced to 7.70 ps for BA+PVSK/Spiro-OMeTAD film. Thus, the above results confirm that the hot holes can be more efficiently transferred to Spiro-OMeTAD HTL from BA-treated perovskite film before them completely cooling to the perovskite crystal lattice, leading to the improvement of PSCs performance [52,53].

In summary, we have introduced two carbonyl-type organic small molecules of BA and AA into perovskite to explore their influences on the perovskite crystallization and the hot carrier dynamics. Interestingly, the incorporated additives can modulate perovskite crystallization to form high-quality perovskite films. Meanwhile, the C=O groups effectively passivated under-coordinate Pb^{2+} defects *via* strong Lewis-acid interaction, thereby reducing the trap-states density and suppress charge recombination. Consequently, the obtained PCE values of PSCs are 19.41%, 21.52% and 20.50% for control, BA and AA-treated devices, respectively. Among them, the BA-treated device achieves the best efficiency, which is attributed to the better quality of perovskite films and the reduction of charge recombination in device. Furthermore, the unencapsulated BA-treated PSCs show the improved device stability, retaining ~93.7% of initial efficiency after aging for 1160 h, conversely, the control device rapidly drops to 77.1% of its initial PCE after 360 h. More importantly, fs-TA results reveal that the incorporated BA additive can efficiently promote hot holes transfer and extraction at the perovskite/Spiro-OMeTAD interface, resulting in the reduction of charge recombination in device. Hence, these results could provide some insights for in-depth unraveling the structure-activity relationship and the charge-carrier transfer dynamics, which shows the great significance for further boosting the photovoltaic properties of PSCs.

Acknowledgments

Y. Hua thanks National Natural Science Foundation of China (No. 22065038), High-Level Talents Introduction in Yunnan Province (No. C619300A010), the Fund for Excellent Young Scholars of Yunnan (No. 202001AW070008), Spring City Plan: the High-level Talent Promotion and Training Project of Kunming (No. 2022SCP005) for financial support. R. J. Zhao thanks the support from the Postdoctoral Research Foundation of Yunnan University (No. W8223004) and the Postdoctoral Foundation of Department of Human Resources and Social Security of Yunnan Province (No. C615300504046).

Supplementary materials

Supplementary material associated with this article can be found, in the online version, at doi:10.1016/j.cclet.2024.109587.

References

[1] G.C. Xing, N. Mathews, S. Sun, et al., Science 342 (2013) 344–347.
[2] J.S. Huang, Y.B. Yuan, Y.C. Shao, Y.F. Yan, Nat. Rev. Mater. 2 (2017) 17042.
[3] J.J. Yoo, G. Seo, M.R. Chua, et al., Nature 590 (2021) 587–593.
[4] T.H. Yang, L.L. Gao, J. Lu, et al., Nat. Commun. 14 (2023) 839.
[5] Q.F. Dong, Y.J. Fang, Y.C. Shao, et al., Science 347 (2015) 967–969.
[6] X.D. Li, W.X. Zhang, X.M. Guo, et al., Science 375 (2022) 434–437.
[7] W.Y. Cao, Z.S. Hu, Z.H. Lin, et al., J. Energy Chem. 68 (2022) 420–438.
[8] National Renewable Energy Laboratory, Best research-cell efficiencies chart, https://www.nrel.gov/pv/cellefficiency.html, 2023.
[9] Y.C. Shao, Z.G. Xiao, C. Bi, Y.B. Yuan, J.S. Huang, Nat. Commun. 5 (2014) 5784.
[10] D. Shi, V. Adinolfi, R. Comin, et al., Science 347 (2015) 519–522.
[11] K. Cao, Y. Huang, M.R. Ge, et al., ACS Appl. Mater. Interfaces 13 (2021) 26013–26022.
[12] S. Cacovich, G. Vidon, M. Degani, et al., Nat. Commun. 13 (2022) 2868.
[13] A.E. Shalan, E. Akrman, F. Sadegh, S. Akin, J. Phys. Chem. Lett. 12 (2021) 997–1004.
[14] D.Y. Luo, R. Su, W. Zhang, Q.H. Gong, R. Zhu, Nat. Rev. Mater. 5 (2020) 44.
[15] Q. Jiang, Z.M. Chu, P.Y. Wang, et al., Adv. Mater. 29 (2017) 1703852.
[16] J.K. Zhang, H.Z. Yu, J. Energy Chem. 54 (2021) 291–300.
[17] T. Wu, R.J. Zhao, D.L. Jia, et al., J. Energy Chem. 77 (2023) 514–520.
[18] Y. Zhao, F. Ma, Z.H. Qu, et al., Science 377 (2022) 531–534.
[19] X.Y. Yu, D.P. Gao, Z. Li, et al., Angew. Chem. Int. Ed. 62 (2023) e202218752.
[20] L.J. Zhu, Q.P. Lu, C.H. Li, Y. Wang, Z.B. Deng, Chin. Chem. Lett. 32 (2021) 2259–2262.
[21] Y.H. Wu, Q. Wang, Y.T. Chen, W.K. Qiu, Q. Peng, Energy Environ. Sci. 15 (2022) 4700–4709.
[22] X.C. Li, X. Wu, B. Li, et al., Energy Environ. Sci. 15 (2022) 4813–4822.
[23] M.H. Li, J.J. Zhou, L.G. Tan, et al., The Innovation 3 (2022) 100310.
[24] X.J. Zhu, M.Y. Du, J.S. Feng, et al., Angew. Chem. Int. Ed. 60 (2021) 4238–4244.
[25] X.F. Xia, J.Y. Peng, Q.X. Wan, et al., ACS Appl. Mater. Interfaces 13 (2021) 17677–17689.
[26] M.G. Li, H. Gao, L.S. Yu, et al., Small 17 (2021) 2102090.
[27] L.Q. Zhu, R.J. Zhao, R.S. Zhuang, et al., EcoMat 5 (2023) e12313.
[28] R.N. Yu, G.Z. Wu, R. Shi, et al., Adv. Energy Mater. 13 (2023) 2203127.
[29] W.J. Zhao, J. Xu, K. He, et al., Nano-Micro Lett. 13 (2021) 169.
[30] L.H. Zhu, X. Zhang, M.J. Li, Adv. Energy Mater. 11 (2021) 2100529.
[31] E. Khorshidi, B. Rezaei, A. Kavousighahfarokhi, et al., ACS Appl. Mater. Interfaces 14 (2022) 54623–54634.
[32] R. Su, X.D. Yang, W.X. Ji, et al., J. Mater. Chem. C 10 (2022) 18303–18311.
[33] J. Peng, J.I. Khan, W.Z. Liu, et al., Adv. Energy Mater. 8 (2018) 1801208.
[34] C. Liu, S. Liu, Y.F. Wang, et al., Adv. Funct. Mater. 31 (2021) 2010603.
[35] J. Yoon, X.W. Liu, E.-C. Lee, ACS Omega 7 (2022) 34278–34285.
[36] C.H. Duan, Z.H. Liang, J.G. Cao, et al., ACS Appl. Mater. Interfaces 14 (2022) 43298–43307.
[37] R.J. Zhao, T. Wu, R.S. Zhuang, Y. Hua, Y.D. Wang, Energy Environ. Mater. (2022) e12417.
[38] Y.B. Li, F. Wu, M.M. Han, et al., ACS Energy Lett. 6 (2021) 869–876.
[39] S.H. Wang, H.Q. Luo, Z.K. Gu, et al., Adv. Funct. Mater. (2023) 2214834.
[40] Y.T. Cheng, Q.B. Wei, N.N. Wang, et al., Chin. Chem. Lett. 34 (2023) 107933.
[41] W. Tress, M. Yavari, K. Domanski, et al., Energy Environ. Sci. 11 (2018) 151–165.
[42] R. Azmi, S.H. Oh, S.Y. Jang, ACS Energy Lett. 1 (2016) 100–106.
[43] H. Li, L.M. Tao, F.L. Huang, et al., ACS Appl. Mater. Interfaces 9 (2017) 38967–38976.
[44] A. Abate, M. Saliba, D.J. Hollman, et al., Nano Lett. 14 (2014) 3247–3254.
[45] I. Dursum, P. Maity, J. Yin, et al., Adv. Energy Mater. 9 (2019) 1900084.
[46] J.H. Fu, Q. Xu, G.F. Han, et al., Nat. Commun. 8 (2017) 1300.
[47] Q. Wei, J. Yin, Q.M. Bakr, et al., Angew. Chem. Int. Ed. 60 (2021) 10957.
[48] G. Ghosh, K. Marjit, S. Ghosh, et al., J. Phys. Chem. C 125 (2021) 5859–5869.
[49] J. Yin, R. Naphade, P. Maity, et al., Nat. Commun. 12 (2021) 3995.
[50] M.J. Li, S. Bhaumik, T.W. Goh, et al., Nat. Commun. 8 (2017) 14350.
[51] T. Wu, R.J. Zhao, J.M. Qiu, et al., Adv. Funct. Mater. 32 (2022) 2204450.
[52] A.O. El-Ballouli, O.M. Bakr, O.F. Mohammed, J. Phys. Chem. Lett. 11 (2020) 5705–5718.
[53] S. Narra, E. Jokar, O. Pearce, et al., J. Phys. Chem. Lett. 11 (2020) 5699–5704.